Monthly Notices of the ROYAL ASTRONOMICAL SOCIETY

MNRAS **527,** 8043–8053 (2024) https://doi.org/10.1093/mnras/stad3752
Advance Access publication 2023 December 5

General relativistic simulations of high-mass binary neutron star mergers: rapid formation of low-mass stellar black holes

Kutay A. Çokluk [1,2]★ Kadri Yakut[1,2] and Bruno Giacomazzo[3,4,5]

[1] *Department of Astronomy and Space Sciences, Faculty of Science, Ege University, 35100 İzmir, Turkey*
[2] *Ege Gravitational Astrophysics Research Group (eGRAVITY), Ege University, 35100 İzmir, Turkey*
[3] *Dipartimento di Fisica G. Occhialini, Università di Milano – Bicocca, Piazza della Scienza 3, I-20126 Milano, Italy*
[4] *INFN, Sezione di Milano-Bicocca, Piazza della Scienza 3, I-20126 Milano, Italy*
[5] *INAF, Osservatorio Astronomico di Brera, Via E. Bianchi 46, I-23807 Merate, Italy*

Accepted 2023 December 1. Received 2023 November 19; in original form 2023 September 27

ABSTRACT

Almost a hundred compact binary mergers have been detected via gravitational waves by the LIGO-Virgo-KAGRA collaboration in the past few years providing us with a significant amount of new information on black holes and neutron stars. In addition to observations, numerical simulations using newly developed modern codes in the field of gravitational wave physics will guide us to understand the nature of single and binary degenerate systems and highly energetic astrophysical processes. We here presented a set of new fully general relativistic hydrodynamic simulations of high-mass binary neutron star systems using the open-source EINSTEIN TOOLKIT and LORENE codes. We considered systems with total baryonic masses ranging from 2.8 $M_\odot$ to 4.0 $M_\odot$ and used the SLy equation of state. We analysed the gravitational wave signal for all models and report potential indicators of systems undergoing rapid collapse into a black hole that could be observed by future detectors like the Einstein Telescope and the Cosmic Explorer. The properties of the post-merger black hole, the disc and ejecta masses, and their dependence on the binary parameters were also extracted. We also compared our numerical results with recent analytical fits presented in the literature and provided parameter-dependent semi-analytical relations between the total mass and mass ratio of the systems and the resulting black hole masses and spins, merger frequency, BH formation time, ejected mass, disc mass, and radiated gravitational wave energy.

Key words: gravitational waves – hydrodynamics – methods: numerical – software: simulations – neutron star mergers.

1 INTRODUCTION

Since the first binary black hole merger observations detected by the LIGO-Virgo collaboration (Abbott et al. 2016), a new window has been opened in astrophysics in the gravitational wave (GW) field (Barack et al. 2019). In 2017, for the first time, the GW signal from a binary neutron star (BNS) merger, named GW170817, was also detected (Abbott et al. 2017a) and it was accompanied by electromagnetic (EM) counterpart observations from gamma-rays to radio (Abbott et al. 2017b). Thus, the multimessenger era has begun. Two years after the first detection of a BNS merger, GW190425, a new BNS system, was detected by the LIGO-Virgo collaboration (Abbott & et al. 2020). For the latter, there is however no detected EM counterpart. GW190425 observation is significant due to being the heaviest BNS system ever observed, with a total mass ($3.4^{+0.3}_{-0.1} M_\odot$ assumption of high-spin prior) much larger than the one measured for the Galactic BNS systems to date (Farrow, Zhu & Thrane 2019; Zhang et al. 2019).

The possible outcomes of a BNS merger can be either a prompt collapse to a black hole (BH), or the formation of a short-lived hypermassive neutron star (HMNS) or long-lived supramassive neutron star (SMNS) that eventually collapses to a BH, or a stable NS (Piro, Giacomazzo & Perna 2017). If the total gravitational mass of the system, M, is higher than a threshold mass, $M_{\rm thres}$ (e.g. Hotokezaka et al. 2011; Bauswein, Baumgarte & Janka 2013; Barack et al. 2019; Köppel, Bovard & Rezzolla 2019; Kashyap et al. 2022; Perego et al. 2022), then the remnant of the merger will promptly collapse to a BH. Although from the Galactic population of BNSs the masses of NSs in BNS systems are expected to lie in a range 1.3–1.4 $M_\odot$, studies (Margalit & Metzger 2019; Paschalidis & Ruiz 2019) suggests, respectively, that up to 25 per cent and 32 per cent of BNS mergers might produce a rapid collapse to BH. For GW190425, it is estimated that the probability of the binary promptly collapsing into a BH after the merger is 96 per cent, with the low-spin prior, or 97 per cent with the high-spin prior (Abbott & et al. 2020).

BNS simulations in recent years (see e.g. Shibata, Taniguchi & Uryū 2003, 2005; Shibata & Taniguchi 2006; Kiuchi et al. 2009; Rezzolla et al. 2010; Hotokezaka et al. 2013; Kastaun et al. 2013; East et al. 2016; Endrizzi et al. 2016; Dietrich et al. 2017a, b; Endrizzi et al. 2018; East et al. 2019; Most et al. 2019; Paschalidis & Ruiz 2019; Ruiz et al. 2019; Ruiz, Tsokaros & Shapiro 2020; Tootle et al. 2021; Papenfort et al. 2022; Sun et al. 2022) have revealed that the amount of disc mass surrounding BH and the amount of ejected matter from the system are strongly dependent on the mass of the system, mass ratio, equation of state (EOS), spin, and magnetic field

★ E-mail: kutay.arinc.cokluk@ege.edu.tr

Table 1. We list the BNS systems studied in this paper. The first column lists the model names, e.g. `M32q10` refers to a BNS system with a total baryonic mass of $3.2M_\odot$ and mass ratio $q = 1.0$. While $M_{1b,\,2b}$ represent the baryonic mass of the components, $M_{1,\,2}$ are the gravitational mass of each neutron star at infinite separation. M_0, J_0, and f_0 are, respectively, the total initial ADM mass, the total initial angular momentum, and initial orbital frequency of the system. The last three columns show the compactness parameters of each NS and the combined dimensionless tidal deformability $\widetilde{\Lambda}$, all computed at infinite separation.

Model	M_{1b} $[M_\odot]$	M_{2b} $[M_\odot]$	M_1 $[M_\odot]$	M_2 $[M_\odot]$	M_0 $[M_\odot]$	J_0 $\left[\frac{GM_\odot^2}{c}\right]$	f_0 [Hz]	C_1	C_2	$\widetilde{\Lambda}$
`M28q10`	1.40	1.40	1.28	1.28	2.54	6.41	324.64	0.161	0.161	511.90
`M30q10`	1.50	1.50	1.36	1.36	2.70	7.11	332.41	0.172	0.172	343.70
`M30q11`	1.57	1.43	1.42	1.30	2.70	7.09	332.38	0.179	0.164	347.14
`M32q10`	1.60	1.60	1.44	1.44	2.85	7.83	339.64	0.182	0.182	234.21
`M32q11`	1.68	1.52	1.50	1.38	2.85	7.81	339.49	0.191	0.174	236.73
`M32q12`	1.75	1.45	1.56	1.32	2.85	7.77	339.39	0.198	0.167	243.35
`M32q13`	1.81	1.39	1.61	1.27	2.85	7.70	339.23	0.206	0.160	253.33
`M32q14`	1.87	1.33	1.65	1.22	2.85	7.62	339.11	0.212	0.153	265.62
`M32q16`	1.97	1.13	1.73	1.14	2.85	7.42	338.64	0.224	0.142	297.33
`M32q18`	2.06	1.14	1.79	1.06	2.85	7.21	338.07	0.235	0.133	335.11
`M32q20`	2.13	1.07	1.85	1.00	2.85	6.98	337.76	0.244	0.124	377.94
`M34q10`	1.70	1.70	1.52	1.52	3.01	8.51	346.16	0.193	0.193	161.02
`M36q10`	1.80	1.80	1.60	1.60	3.16	9.33	352.37	0.205	0.205	111.01
`M36q11`	1.89	1.71	1.66	1.53	3.16	9.31	352.45	0.214	0.195	112.51
`M38q10`	1.90	1.90	1.68	1.68	3.31	10.11	358.42	0.216	0.216	76.46
`M38q11`	1.99	1.81	1.74	1.61	3.31	10.09	358.25	0.226	0.206	77.61
`M40q10`	2.00	2.00	1.75	1.75	3.46	10.90	363.73	0.228	0.228	52.19
`M40q11`	2.10	1.90	1.82	1.68	3.46	10.88	363.83	0.239	0.216	53.00

of neutron stars. In addition, the effects of the BNS mass, mass ratio, EOS, spin, and magnetic field constitute a highly degenerate parameter space, which makes precise arguments difficult to make, as long as simulations that include all of the above are still lacking. Because nearly all matter is swallowed by the remnant BH, it is expected that equal-mass BNS systems with $M{>}M_{\rm thres}$ will have a disc with negligible mass and a low amount of ejected matter.

High-mass mergers, such as the ones discussed in this study, are important to study because they can provide insight into high-mass neutron stars and the remnants produced by their mergers. We can also learn about the internal structure of massive neutron stars (e.g. their EOS) by analysing these types of mergers. We conducted simulations of high-mass binary systems that underwent rapid collapse in this study, and we investigated the effects of mass ratio and total mass on gravitational wave emission and system dynamics. The paper is organized as follows: we review the numerical setup and initial data for our models in Section 2. The numerical results are presented in Section 3. Finally, we discuss our findings in Section 4. We use a system of units in which $c = G = \mathrm{M}_\odot = 1$, unless specified otherwise.

2 MODELS AND NUMERICAL SETUPS

We consider a set of irrotational equal and unequal mass BNS systems with a total baryonic mass between 2.8 and 4.0 $\mathrm{M}_\odot$. We computed the initial data using the pseudo-spectral elliptic solver `LORENE` (Gourgoulhon et al. 2001; Gourgoulhon et al. 2016) assuming irrotational NSs on a quasi-circular orbit. For all models, the initial coordinate separation is 40 km, corresponding to $\approx$3 orbits before merger. We report the initial parameters of our models in Table 1. The first column refers to the names of the models, e.g. `M32q10` means that the initial total baryonic mass of the BNS is 3.2 $\mathrm{M}_\odot$ and that the mass ratio is 1.0 (the mass ratio is defined such that $q = M_{1b}/M_{2b} > 1$). From second to fifth columns we show, respectively, neutron stars' initial baryonic masses ($M_{1b,\,2b}$) and gravitational ($M_{1,\,2}$) masses at infinite separation. M_0, J_0, and f_0 are the values of the initial ADM mass, total angular momentum, and orbital frequency. The compactness parameters of each NS are given as $C_{1,\,2}$ where $C_{1,\,2} = GM_{1,\,2}/R_{1,\,2}c^2$ and C_1 and C_2 are computed considering the NS at infinite separation. The last column refers to the reduced tidal parameter, $\widetilde{\Lambda}$ (Favata 2014):

$$\widetilde{\Lambda} = \frac{16}{13}\frac{(M_1 + 12M_2)}{M^5}\Lambda_1 M_1^4 + (1 \rightarrow 2)\,, \tag{1}$$

where the quadrupolar tidal parameter of the individual stars (Flanagan & Hinderer 2008; Damour & Nagar 2010) is $\Lambda_i = \frac{2}{3}C_i^{-5}k_i^{(2)}$, $i = 1, 2$, and $k_i^{(2)}$ is the dimension-less Love number (Damour 1983; Hinderer 2008; Binnington & Poisson 2009; Damour & Nagar 2009). The notation $(1 \rightarrow 2)$ indicates a second term identical to the first, but 1 and 2 are exchanged.

This work employs the SLy EOS (Douchin & Haensel 2001) to describe the NS matter. To build the initial data, we used the EOS table provided by Parma Gravity Group.[1] During the evolution, we instead used the seven piece polytropic version (SLyPP) described in De Pietri et al. (2016) and added a thermal component given by $\Gamma_{\rm thermal} = 1.8$.

To solve the general relativistic hydrodynamic (GRHD) equations, we used the publicly available `EINSTEIN TOOLKIT` (ET) (Löffler et al. 2012; Etienne et al. 2021) code, based on `CACTUS COMPUTATIONAL TOOLKIT`.[2] In particular, we used the nineteenth release version of ET named 'Katherine Johnson' (ET_2021_11) (Brandt et al. 2021).

We evolve the space–time metric using the BSSN formalism (Nakamura, Oohara & Kojima 1987; Shibata & Nakamura 1995; Baumgarte & Shapiro 1998; Alcubierre et al. 2000, 2003) as implemented in the `McLachlan` thorn.[3] We use the `GRHydro`

[1] https://bitbucket.org/GravityPR
[2] http://www.cactuscode.org/
[3] http://www.cct.lsu.edu/ eschnett/McLachlan

code (Baiotti et al. 2005; Hawke, Löffler & Nerozzi 2005; Mösta et al. 2013) to solve the GRHD equations and employ a fifth-order WENO-Z reconstruction method (Borges et al. 2008). The time integration is handled with a fourth-order Runge–Kutta method (Runge 1895; Kutta 1901) with a Courant factor of 0.4. We also set an artificial atmosphere of $\rho_{\rm atm} = 1.01 \times 10^{-11}$. We also would like to state that the value of $\rho_{\rm atm}/\rho_{\rm max}$ for the less massive companion, which is from model `M32q20` and has 1.07 $M_\odot$ baryonic mass, is 9.08×10^{-9}.

We employ an adaptive mesh refinement (AMR) approach provided by the `Carpet` driver (Schnetter, Hawley & Hawke 2004) and we force the finest grids to follow each NS during the inspiral. The grid hierarchy consists of seven nested refinement levels with a 2:1 refinement factor. The resolution of each simulation is characterized by the resolution of the innermost grid, which is $dx = 0.16 \approx 237$ m, while the radius of the outer boundary of the numerical domain is $1024 \approx 1514$ km. We apply reflection symmetry along the z=0 plane. After merger, if the final remnant's mass exceeds the EOS's threshold mass, the `AHFinderDirect` thorn (Thornburg 2003) is used to detect the formation of an apparent horizon and extract the properties of the BH.

Note that results presented in this paper are extracted from the simulations having the standard resolution (SR) of $dx = 0.16$. For two models, we also run a high resolution (HR) and low resolution (LR) simulations with $dx = 0.12$ and $dx = 0.20$ in order to estimate our numerical error. The accuracy of our results is discussed in Appendix A.

3 RESULTS

3.1 GW extraction and analysis

We computed the GWs from −7 ms to 10 ms, where $t = 0$ ms corresponds to the maximum strain amplitude and refers to the merger time, and the GWs include approximately the last three orbits before merger.

We extract the GW signal at a coordinate radius of ≈ 444 km from the BNS centre-of-mass, calculating the Newman–Penrose scalar ψ_4 (Newman & Penrose 1962) (equation 2), provided by ET module `WeylScal4`, and decomposed in spin-weighted spherical harmonics using the ET module `Multipole`:

$$\ddot{h}_+ - \ddot{h}_\times = \psi_4 = \sum_{l=2}^{\infty} \sum_{m=-l}^{l} \psi_4^{lm}(t, r)\ {}_{-2}Y_{lm}(\theta, \phi). \tag{2}$$

Since ψ_4 is the second time derivative of the GW strain, it is required to integrate it twice in time to obtain h_{lm}. For the time integration and further GW signal analysis, we used a publicly available `PYTHON` module, `Kuibit` (Bozzola 2021), and computed h_+ and h_x with equation (3) via the FFI method described in Reisswig & Pollney (2011):

$$h_+^{lm}(r, t) - i h_\times^{lm}(r, t) = \int_{-\infty}^{t} du \int_{-\infty}^{u} dv\ \psi_4^{lm}(r, v) \tag{3}$$

For all of our GW analysis, the complex combination of the extracted GW amplitude polarizations, $h = h_+ - ih_\times$, is used, and only the dominant mode, i.e. $l = m = 2$, is considered. Note that the h_{22} mode we extracted from the simulation is the amplitude of the (2,2) mode without the spherical harmonics term. Therefore it does not take into account the effect of the viewing angle. We also plot the waveform as a function of retarded time (equation 4), where the areal radius is $R = \sqrt{A(r)/4\pi}$, and $A(r)$ is the surface of the sphere of coordinate radius (r):

$$t_{\rm ret} = tR - 2M_0 \log(\frac{R}{2M_0} - 1). \tag{4}$$

The instantaneous frequency of GW is computed as

$$f_{\rm GW} = \frac{1}{2\pi} \frac{d\phi}{dt}, \tag{5}$$

where $\phi = \arctan(h_\times/h_+)$ is the phase of the GW signal. The frequency at merger is $f_{\rm merger} = f_{GW}(t = 0)$.

The GW strain (upper) and the phase velocity (bottom) for equal (left) and unequal (right) mass models are shown in Fig. 1. Gravitational waveforms include the last part of inspiral, approximately three orbits before merger, and the coalescence and ringdown stages for all models. Models with larger total mass show, as expected, higher GW amplitudes at merger, while models with higher mass ratios have smaller amplitudes.

Because of the prompt formation of a BH, all GW signals go to zero less than ≈2 ms after the merger. The frequency evolution for all models is shown in the bottom panels. Before the merger stage, the frequencies are nearly identical for all models and increase monotonically with GW amplitude in time. Except for high mass ratio models, the frequency increases after merger due to increased compactness and faster rotation of the remnant, as explained in Endrizzi et al. (2016) and Kastaun, Ciolfi & Giacomazzo (2016). They behave differently for the latter in that, while model `M32q20` oscillates around 1 kHz, the frequencies of the other models rapidly increase shortly before 1 ms.

We then compute the amplitude spectral density (ASD) as $2|\bar{h}(f)|f^{1/2}$, where $\bar{h}(f) = \sqrt{\frac{|\bar{h}_+(f)|^2 + |\bar{h}_\times(f)|^2}{2}}$, where $\bar{h}_+$ and $\bar{h}_\times$ are the Fourier transforms of h_+^{22} and $h_\times^{22}$ computed from the beginning of the simulations up to 10 ms after merger. Fig. 2 shows the amplitude spectral density of the GW signals for equal (left panel) and unequal (right panel) models placed at a distance of 50 Mpc and the sensitivity curves of current (aLIGO+, KAGRA) and future planned (Einstein Telescope, Voyager, Cosmic Explorer) detectors. The initial frequency peak at around 1000 Hz is equal to the double of the initial orbital frequency of each model, and it just indicates the beginning of the inspiral stages in our simulations. From Fig. 2 we can see that all systems can be observed in their merger phase by all detectors but KAGRA (which would be able to see only the earlier part of the inspiral, not simulated here).

Besides, we observe plateaus between 4000 and 7000 Hz for all models, but `M38q10` and `M40q10` which are those that form a BH earlier. For the unequal-mass models, the frequency of plateaus changes with the mass ratio and are more evident for larger mass ratios. Moreover, we realize that frequencies of plateaus show a turning point. While a more noticeable plateau is observed in models with higher mass ratios, the clarity decreases as we move towards models with equal mass. Moreover, plateaus are observed at higher frequencies and higher ASD values as the mass ratios decrease, while the ASD value decreases after $q = 1.0 - 1.2$. This suggests that there is a turning point in this mass ratio range. In Kiuchi et al. (2010) it is suggested that plateaus at high frequencies are related to both the formations and evolution of black holes and of their surrounding discs. Therefore, we compare the ASD of model `M30q10`, which shows delayed collapse into a BH surrounded by torus after a short-lived HMNS phase, and prompt collapse models with torus (e.g. `M32q10`) and without torus (e.g. `M34q10, M36q10`). We realize that those plateaus are only related to the case of prompt collapse models regardless of having a torus or not.

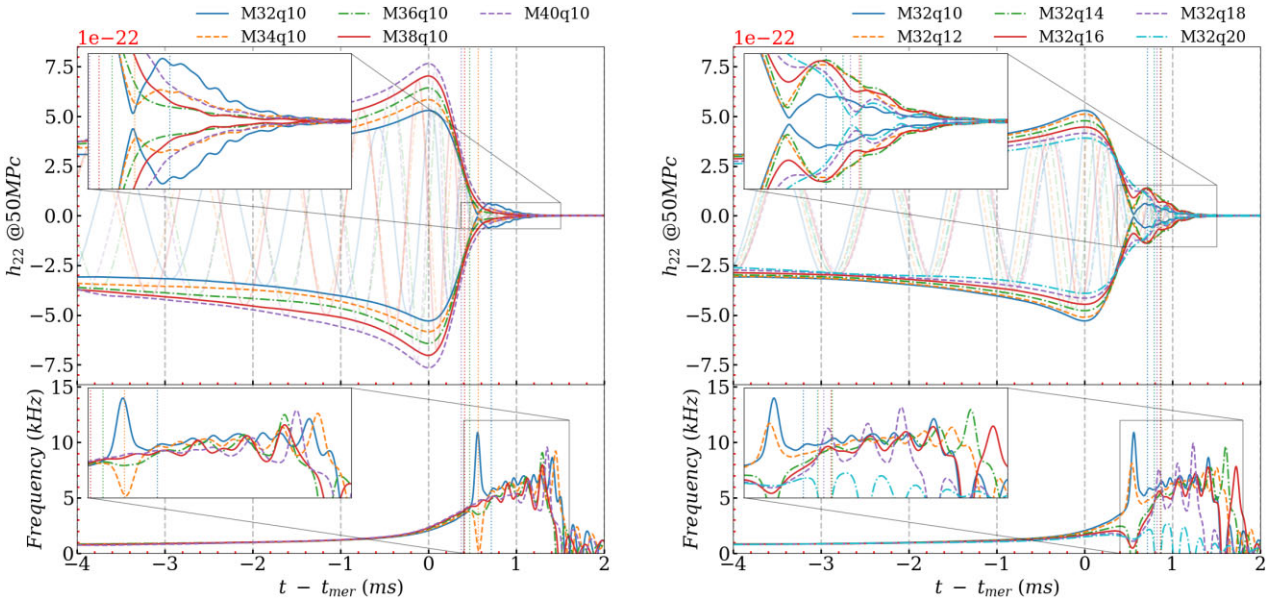

Figure 1. The left and right figures represent, respectively, equal and unequal mass models. Upper panels: extracted gravitational waveforms of the dominant mode (l,m=2,2) computed at $r = 444$ km. The thin lines show the GW signal $h_{22} = h_{+,22}$, while the thick outer lines represent the GW amplitudes, $|h| = \sqrt{|h_+|^2 + |h_\times|^2}$ and it does not take into account the effect of the viewing angle. Bottom panels: instantaneous frequency, i.e. the time derivative of the GW phase of each model. Note that the instantaneous frequency is smoothed by convoluting with a blackman window function in 0.1 ms.

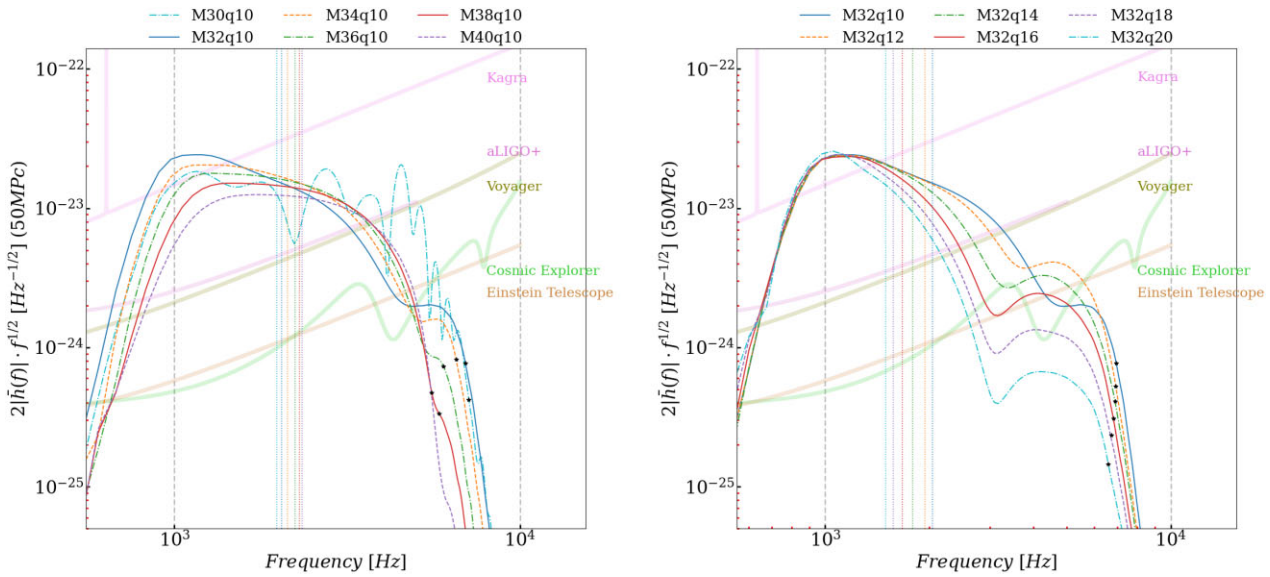

Figure 2. Amplitude spectral densities (ASD) of the GW signals placed at a distance of 50 Mpc. The sensitivity curves of the current and the future-planned detectors (KAGRA, aLIGO+, Voyager, Cosmic Explorer, and Einstein Telescope) are shown as shaded thick lines and they are the ones included in the public version of the `Kuibit PYTHON` library (Bozzola 2021). The vertical dotted lines correspond to the merger frequencies estimated from the instantaneous frequency at merger. The quasi-normal-mode frequencies of the final black holes are marked with black star markers.

We calculated the quasi-normal-mode frequencies of the corresponding BH mass and spin using equation (6) from Nakamura, Oohara & Kojima (1987).

$$f_{qnm} \approx 10.8 \left(\frac{M}{3\,M_\odot}\right)^{-1} [1 - 0.63(1-\chi)^{-0.3}]\,\text{kHz}. \quad (6)$$

According to Kiuchi et al. (2010), peak frequency and width of plateu show correlation with the disc mass. Thus, these plateaus provide us with an information about the formation and evolution of matter around the central object. If the frequency increases, we observe a decrease in the amplitude spectral density, as expected, due to the QNM ring-down of the formed BH. In Fig. 2, the black star marks show the QNM ring-down frequencies for each model.

3.2 Remnant properties

We consider the matter whose time-component of the four-velocity is $u_t < -1$ as ejected matter, and we indicate its mass as $M_{\rm ejec}$. We also

Table 2. We report the values of numerical results from the standard resolution (SR) simulations and the value inside brackets (third row) shows the error on the last digit as the absolute semi-difference between low resolution (LR) and high resolution (HR) simulations, except for the disc and ejecta masses where we provide the relative errors. Details on the estimates of such errors can be found in Appendix A. The second column shows the instantaneous frequency at merger, $f_{\rm merger}$, corresponding to the maximum GW amplitude. The third column is the elapsed time, $t_{\rm BH}$, from the merger to the formation of BH. $M_{\rm rem}$ is the mass of the remnant. If the remnant is a BH, it is a quasi-local measure mass, otherwise, it is the ADM mass of the remnant NS. The fifth to last columns represent, respectively, dimension-less spin of the BH, $\chi_{\rm BH}$, the disc mass, $M_{\rm disc}$, the amount of ejected matter, $M_{\rm ejec}$ and total radiated energy in GW, $E_{\rm GW}$.

Model	$f_{\rm merger}$ (kHz) (2)	$t_{\rm BH}$ (ms) (1)	$M_{\rm rem}$ ($\rm M_\odot$) (1)	$\chi_{\rm BH}$ (J/M^2) (6)	$M_{\rm disc}$ (10^{-3} $\rm M_\odot$) (36 per cent)	$M_{\rm ejec}$ (10^{-3} $\rm M_\odot$) (96 per cent)	$E_{\rm GW}$ ($\rm M_\odot c^2$) (2)
M28q10	1.87	–	2.133	–	660	2	0.065
M30q10	1.98	2.61	2.613	0.727	20	7	0.056
M30q11	2.01	–	2.225	–	800	20	0.063
M32q10	2.05	0.72	2.823	0.790	0.11	0.03	0.029
M32q11	2.01	0.75	2.818	0.789	3	0.8	0.030
M32q12	1.94	0.79	2.802	0.779	17	6	0.029
M32q13	1.86	0.84	2.777	0.766	40	12	0.026
M32q14	1.79	0.87	2.760	0.756	60	11	0.023
M32q16	1.67	0.86	2.722	0.726	95	9	0.019
M32q18	1.57	0.83	2.700	0.698	108	11	0.015
M32q20	1.50	0.79	2.680	0.663	113	17	0.013
M34q10	2.13	0.57	2.973	0.779	–	–	0.034
M36q10	2.24	0.47	3.118	0.768	–	–	0.042
M36q11	2.20	0.48	3.118	0.769	–	–	0.041
M38q10	2.30	0.42	3.258	0.754	–	–	0.051
M38q11	2.27	0.42	3.258	0.755	–	–	0.050
M40q10	2.34	0.37	3.393	0.741	–	–	0.061
M40q11	2.33	0.38	3.394	0.741	–	–	0.059

define the disc mass as the baryonic mass of regions with rest mass density above the artificial atmosphere, $\rho_{\rm atm} = 6.2 \times 10^6 \rm g\,cm^{-3}$, and that are not ejected (i.e. we exclude $M_{\rm ejec}$ from the disc mass). Besides, to consider effects of artificial atmosphere's density to disc mass and ejected matter, we simulated model of `M32q10` with three different atmosphere density. Details given in Appendix A.

All simulations run in this study result in the rapid collapse into a BH, except `M2810, M30q11` (hyper-massive NS), and `M30q10` (delayed collapse into a BH). In Table 2 we report the formation time of the BH after merger. As seen from the values of $t_{\rm BH}$, all promptly collapse models form a BH before 0.9 ms. The results suggest that for massive binary systems, the rapid formation of a BH occurs sooner because there is not enough time for the redistribution of angular momentum to support the remnant, resulting in an earlier collapse into a BH. As suggested in Shibata, Taniguchi & Uryū (2003) and Shibata & Taniguchi (2006), nearly all the matter tends to fall into the BH in the prompt collapse scenario. Moreover, it is realized that the elapsed time for the formation of a BH changes in a parabolic way with the increase of the mass ratio. When the mass ratio is between $q = 1.0 - 1.4$, the required time to form a BH increases, but after $q = 1.4$, it starts to decrease.

We report the final mass and dimension-less spins of BH found by `AHFinder` after the merger in Table 2. The final black hole swallows 94–99 per cent of the initial binary mass. Similarly, we estimate that approximately 70–80 per cent of the initial total angular momentum is transferred to the final BH with dimension-less spin between 0.66 and 0.79 as also suggested in Kiuchi et al. (2009). We also estimated that the energy carried away by gravitational radiation should be between 0.01 and 0.07 $\rm M_\odot c^2$.

Fig. 3 shows the dependence of $f_{\rm merger}$, $t_{\rm BH}$, $M_{\rm BH}$, $E_{\rm GW}$, $M_{\rm disc}$, and $M_{\rm eject}$ on the different initial total mass of the system and mass ratios for the eighteen simulations performed in this study. As it can be seen in Fig. 3, the relationships between some of the parameters are clearly visible.

$$
\begin{aligned}
f_{\rm merger} &= -0.242\, M_b^2 + 2.132\, M_b - 2.316\,(1.5\ \text{per cent}) \\
&= 0.166\, q^2 - 1.070\, q + 2.968\,(1.5\ \text{per cent}) \\
t_{\rm BH} &= 0.491\, M_b^2 - 3.971\, M_b + 8.413\,(1.1\ \text{per cent}) \\
&= -0.469\, q^2 + 1.480\, q - 0.302\,(1.3\ \text{per cent}) \\
M_{\rm BH} &= -0.069\, M_b^2 + 1.212\, M_b - 0.351\,(0.1\ \text{per cent}) \\
&= 0.041\, q^2 - 0.279\, q + 3.069\,(0.6\ \text{per cent}) \\
\chi_{\rm BH} &= -0.017\, M_b^2 + 0.064\, M_b + 0.762\,(0.1\ \text{per cent}) \\
&= -0.059\, q^2 + 0.047\, q + 0.806\,(0.2\ \text{per cent}) \\
E_{\rm GW} &= 0.023\, M_b^2 - 0.127\, M_b + 0.201\,(0.1\ \text{per cent}) \\
&= -0.001\, q^2 - 0.017\, q + 0.049\,(0.1\ \text{per cent}) \\
M_{\rm disc} &= -0.079\, q^2 + 0.366\, q - 0.298\,(0.8\ \text{per cent}) \\
M_{\rm eject} &= -0.013\, q^2 + 0.052\, q - 0.039\,(0.3\ \text{per cent})
\end{aligned}
\tag{7}
$$

We plot in Fig. 3 $\rm E_{GW}$, $\rm M_{eject}$, $\rm M_{disc}$, $\chi_{\rm BH}$, $\rm M_{BH}$, $\rm t_{BH}$, and $\rm f_{merger}$ in function of the initial total baryonic mass of the BNS (M_b) and mass ratio (q) (Table 2). The dashed black curve is a fit to a second-order polynomial using statistical analysis given by equation (7). The uncertainties in the equations are expressed as percentages in

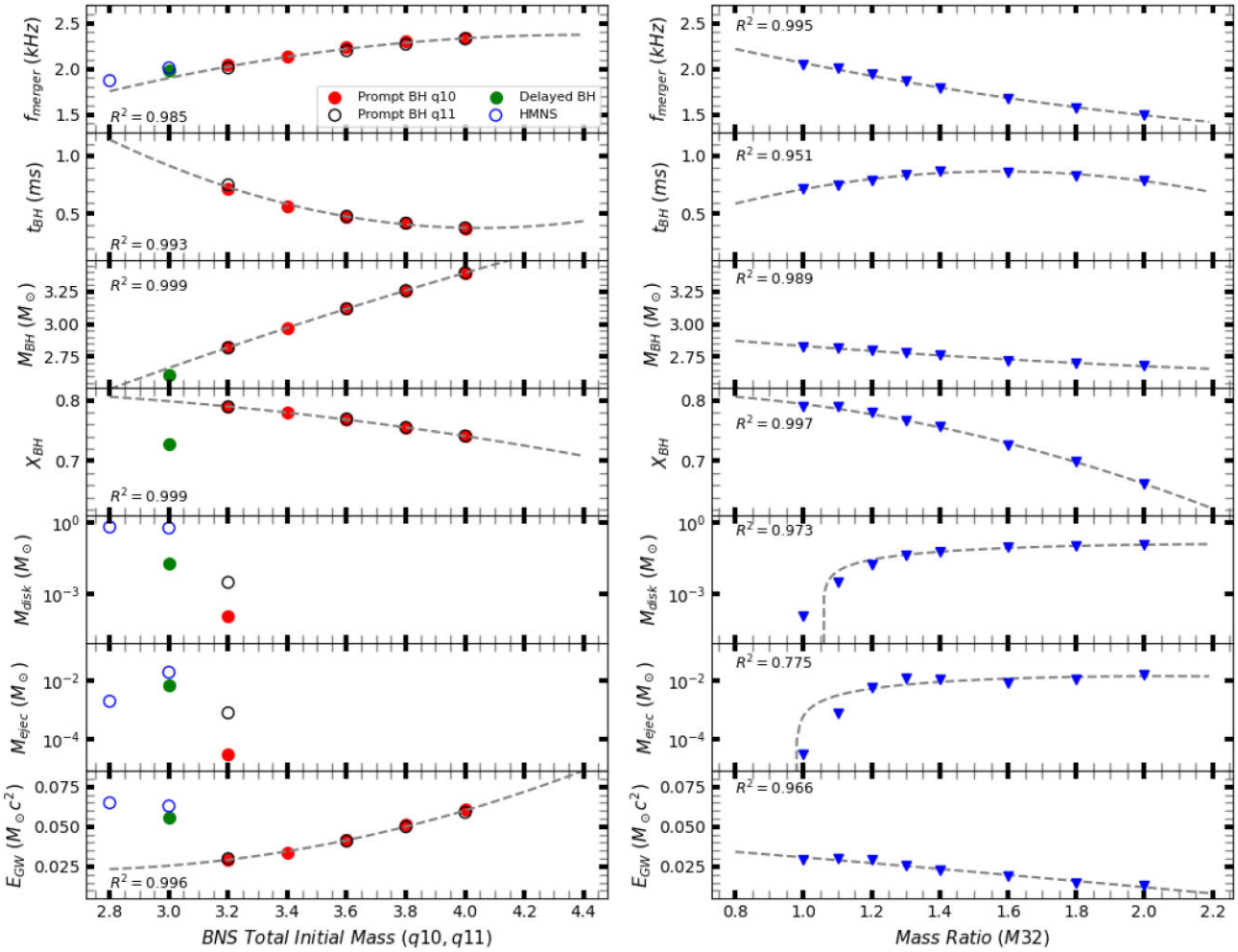

Figure 3. Dependence of the numerical results given in Table 2 from total initial mass (left panels) and mass ratios (right panel). The dashed lines on both plots are fits calculated by considered only results from promptly collapsed models.

parentheses. We believe these relations can be used as a prediction for future simulations using similar equations of state.

In Fig. 3, we show how the values extracted from our simulations change with initial binary neutron star system mass (left panels) and mass ratio (right panels). From the left panels in the figure, it can be seen that the dimension-less spin (mass) of the BH decreases (increases) with increasing BNS mass. When increasing the BNS mass, also the disc mass and the amount of ejected matter from the system decrease. Energy radiated via GW is also increasing for higher mass binary neutron star systems. From these plots, we can estimate that, in the prompt collapse case, the BH swallows $98-99$ per cent of the initial mass of the BNS systems and that the remaining $1-2$ per cent of the initial mass is radiated away from the system as $E_{\rm GW}$. On the other hand, for systems with different mass ratios (right panel of Fig. 3) the final mass of the BH decreases with the increase of mass ratio while the BH spin decreases. Similarly, we observe more massive discs and a higher amount of ejected matter, which are also consistent with the decrease in $E_{\rm GW}$ for higher q.

3.3 Dynamics of systems during evolution

In Fig. 4, we present the evolution of the rest mass density for the equal mass BNS models (`M28q10`, `M30q10`, `M32q10`, and `M34q10`) in the equatorial plane (upper panel) at times -3, 0, 2, 10 ms. The columns indicate times, while the rows refer to the models. All models are inspiralling and losing matter from the tidal tails due to tidal emission 3 ms before the merger (first column in Fig. 4). At $t = 0.00$ ms (second column in Fig. 4), the cores of the two neutron stars merge. Due to the high orbital speed (i.e. high angular momentum), matter is released in a spiral flow. After 2 ms (third column in Fig. 4), we show that `M32q10` and `M34q10` collapse into a BH which rapidly accretes the surrounding matter. However, model `M30q10` shows the formation of a short-lived HMNS right after merger and the formation of a BH 2.6 ms after merger. Similarly, the remnant of `M28q10` is a high-mass neutron star with a thick torus. The comparison of the four models in the figure shows that the disc structure changes with the initial binary mass. The mass of the disc is crucially decreasing for high-mass BNS systems. The bottom panel of Fig. 4 shows the four models on the meridional plane.

Besides, in Fig. 5, we present the evolution of the rest mass density for the BNS system with initial total baryonic mass of $3.2\,{\rm M}_\odot$ and different mass ratios in the equatorial plane (upper panel) at times -3, 0, 2, 10 ms. The rows indicate the models `M32q10`, `M32q13`, `M32q16`, and `M32q20` from up to bottom. The figure shows that models with higher mass ratios produce more massive and extended tidal tails and more matter is released during the inspiral phase. The increment in the amount of released matter is due to the smaller compactness of one of the neutron stars in

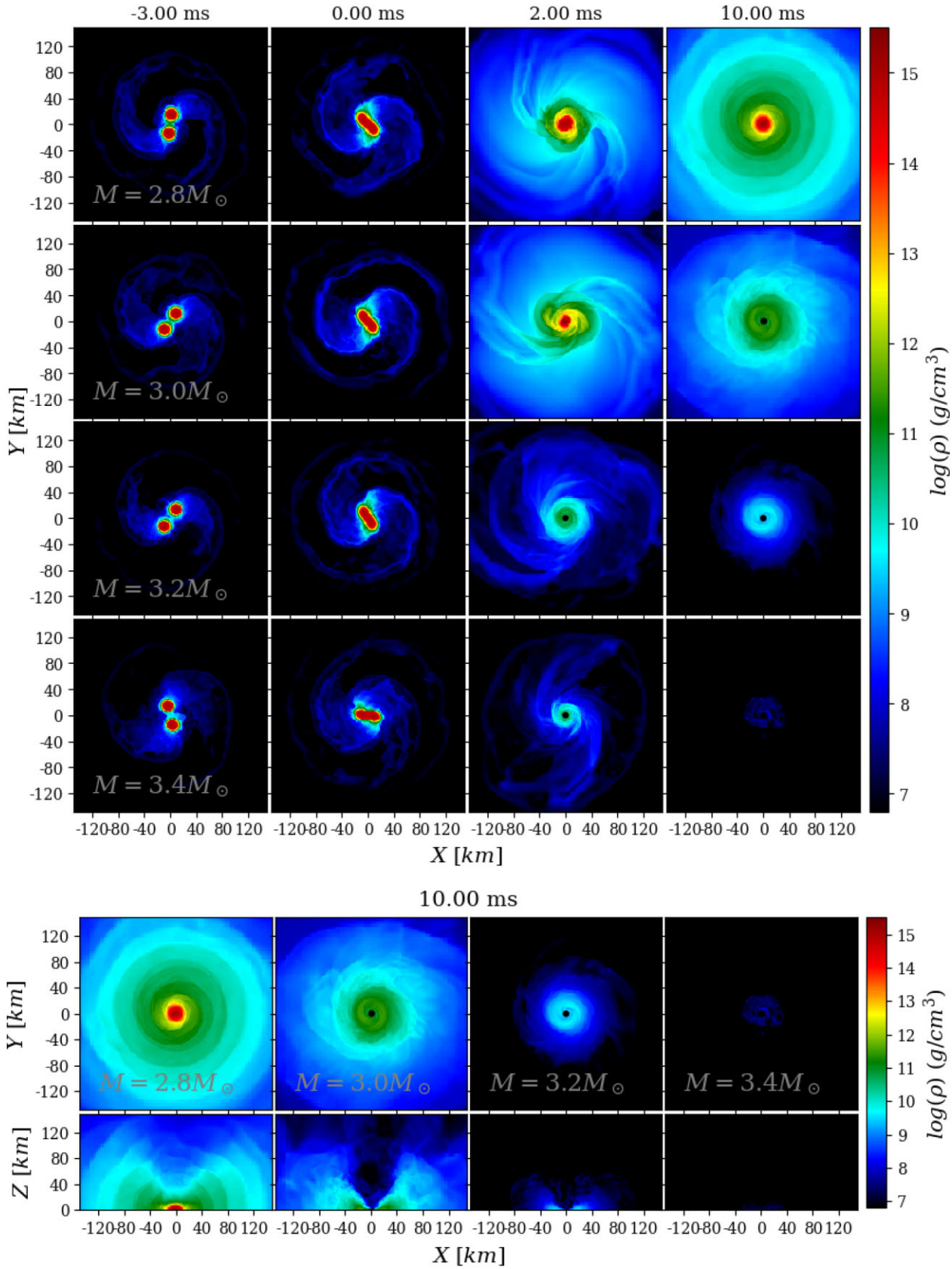

Figure 4. Snapshots of the rest mass density evolution for the equal mass models. Upper panels: the rest-mass density is plotted on the equatorial plane 3 ms before merger, at merger $t = 0$, 2, and 10 ms after merger. Each row represents a different model: top to bottom, `M28q10`, `M30q10`, `M32q10`, and `M34q10`. Bottom panels: comparison of the rest mass density snapshots in the equatorial and meridional planes at the end of the simulations ($t = 10.00$ ms).

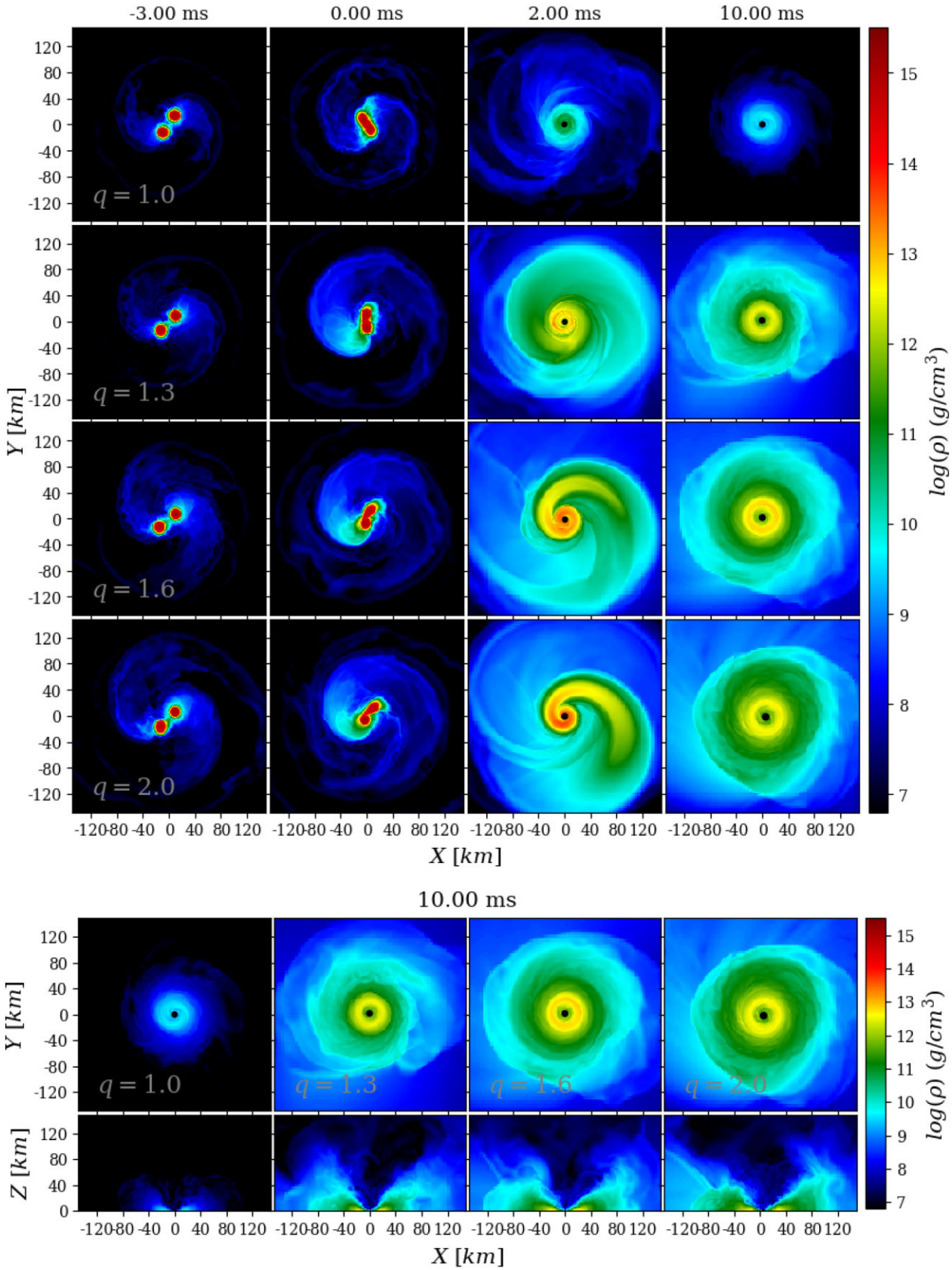

Figure 5. Snapshots of the rest mass density evolution for the unequal mass models. Upper panels: the rest-mass density is plotted on the equatorial plane 3 ms before merger, at merger $t = 0$, 2, and 10 ms after merger. Each row represents a different model: top to bottom, `M32q10`, `M32q13`, `M32q16`, and `M32q20`. Bottom panels: comparison of the rest mass density snapshots in the equatorial and meridional planes at the end of the simulation ($t = 10.00$ ms).

the system, so that the matter from it can be easily unbound. In the case of model M32q20, the less massive NS is swallowed by the more compact one during the coalescence. Due to the less compact NS high orbital speed, there is a one-armed spiral structure around the BH after merger (third column). During this stage, the matter ejected during the merger becomes unbound due to the high angular momentum. At the end of the simulation (fourth column) we can also see how higher mass ratios produce more massive and more extended accretion discs (see also Rezzolla et al. 2010).

The study of Bernuzzi et al. (2020) reports that in the neutron star systems with mass ratios $q = 1.5 - 2$, the massive primary NS tidally disrupts the companion, and the matter of the latter accretes onto the former one. These processes can make the remnant unstable and rapidly collapse into a BH. This process is named accretion-induced prompt collapse in Bernuzzi et al. (2020). Our model, M32q20, shows indeed a rapid accretion-induced collapse to BH.

3.4 Comparison of our results with other works

In the study of Kölsch et al. (2022), the authors used the BAM code to simulate models with three different resolutions: $dx = 0.13,\ 0.16,\ 0.21$, which are closer to the resolutions we used in this study. The models employing the SLy EOS and a gravitational mass of $M = 2.90\,M_\odot$ at different mass ratios ($q = 1.0,\ 1.25$, and 1.50) evolved in Kölsch et al. (2022) are close to our models M32q10 ($M = 2.88$, $q = 1.0$), M32q13 ($M = 2.88$, $q = 1.26$), and M32q16 ($M = 2.88$, $q = 1.52$). We compared the time for the formation of the BH after merger, the BH mass, the BH dimension-less spin, and disc mass. For the models very similar to the M32q10, M32q13, and M32q16, they reported respectively, $M_{\rm BH} = 2.831, \sim 2.784, \sim 2.741\ M_\odot$, $\chi = 0.768, \sim 0.717, \sim 0.657$, and $M_{\rm disc} = 5.6 \times 10^{-4}, \sim 5.346 \times 10^{-2}, \sim 1.145 \times 10^{-1}\ M_\odot$. Besides the differences due to using different resolutions and numerical relativity codes, the values they reported are close to the one we reported in Table 2 in this study.

We also compared our results with current fits available in the literature. For this reason, we used the statistical studies on dynamical ejecta and disc mass in Nedora et al. (2021) to check whether our results are in agreement with their fits. We use in particular the fits for the dynamical ejecta and disc mass listed below (equations 8 and 9):

$$P_2^2(q, \widetilde{\Lambda}) = b_0 + b_1 q + b_2 \widetilde{\Lambda} + b_3 q^2 + b_4 q \widetilde{\Lambda} + b_5 \widetilde{\Lambda}^2\,; \quad (8)$$

$$log_{10}(P_2^2(q, \widetilde{\Lambda})) = log_{10}(b_0 + b_1 q + b_2 \widetilde{\Lambda} + b_3 q^2 + b_4 q \widetilde{\Lambda} + b_5 \widetilde{\Lambda}^2). \quad (9)$$

We use the coefficients recommended in Nedora et al. (2021): $b_0 = -1.32$, $b_1 = -0.382$, $b_2 = -4.47 \times 10^{-3}$, $b_3 = -0.339$, $b_4 = 3.21 \times 10^{-3}$, $b_5 = 4.31 \times 10^{-7}$ for the dynamical ejecta, and $b_0 = -1.85$, $b_1 = 2.59$, $b_2 = 7.07 \times 10^{-3}$, $b_3 = -0.733$, $b_4 = -8.08 \times 10^{-4}$, $b_5 = 2.57 \times 10^{-7}$ for the disc mass.

The results of these formulae are reported in Table 3. Except for model M32q10, the amount of dynamical ejecta we estimated in our simulations agrees with the fits calculated using equation (8). Furthermore, the value of ejected matter from model M32q11 is consistent with the trend. When we compare the disc masses estimated in this study to those estimated with the fit of Nedora et al. (2021), we see that our computed values are always less than the disc mass obtained from the fit. However, such differences may also be related to the various methods and times in which the disc mass was estimated. Moreover, Camilletti et al. (2022) reported that among the four EOSs (BLh, DD2, SFHo, SLy), the SLy EOS used in our simulations provides the lightest disc mass around a central BH. This could also explain the discrepancy between our numerical results and the fit estimates.

Table 3. Relative differences between the fits and our numerical data for the ejected matter and disc mass. $\Delta M = M_{\rm sim} - M_{\rm fit}$ where $M_{\rm sim}$ are the values given in Table 2 as $M_{\rm disc}$ and $M_{\rm eject}$ while $M_{\rm fit}$ are the values computed using equations (8) and (9).

Model	$\Delta M/M_{\rm eject}$	$\Delta M/M_{\rm disc}$
M28q10	− 0.34	− 0.61
M30q10	0.46	− 49.55
M30q11	0.81	− 0.48
M32q10	− 161.34	− 9057.10
M32q11	− 4.66	− 395.03
M32q12	0.31	− 79.98
M32q13	0.68	− 37.69
M32q14	0.68	− 27.12
M32q16	0.63	− 18.26
M32q18	0.75	− 15.25
M32q20	0.84	− 12.18

According to simulations run in Radice et al. (2018) it is proposed that BNS systems with $\widetilde{\Lambda} < 450$ inevitably promptly collapse into a BH and form a surrounding disc $<0.02\,M_\odot$ and that systems with $\widetilde{\Lambda} < 400$ could not be compatible with a lower limit of ejected matter inferred from UV/optical/infrared observations of AT2017gfo, which is the optical counterpart to GW170817. However, it is also stated in Radice et al. (2018) and references therein that mass ratios higher than 1.25 might also form discs with masses up to $0.1\,M_\odot$. According to the outcomes of the models consistent with the chirp mass of GW170817 in this study (M30q10, M30q11, M32q18), models M30q11 and M32q18 with, respectively, $\widetilde{\Lambda} = 335, 347$ may eject at least $0.05\,M_\odot$. Model M30q11 may unbound at least $0.05\,M_\odot$ matter if disc has an ejection efficiency around 5 per cent. For our promptly collapse models, M32q18, this contribution should be at least 35 per cent if we consider the high-spin assumption for GW170817. Therefore, as stated in Kiuchi et al. (2019), we also show that the unequal-mass systems with $\widetilde{\Lambda} < 400$, even if they collapse into a BH promptly, provide both the lower limit of ejected mass, $0.05\,M_\odot$, and disc mass, $0.08\,M_\odot$, reported in Perego, Radice & Bernuzzi (2017). Thus, according to the simulations we run in this study we may confirm that the lower bound on $\widetilde{\Lambda}$ might depend on the mass ratio as suggested in Radice et al. (2018).

4 CONCLUSIONS

We performed a set of equal and unequal high-mass BNS system simulations with seven-segment piecewise polytropic SLy EOS in this study. We started the simulations with three orbits before the merger and followed our systems up to 10 ms after the merger. Except for models M28q10, M30q10, and M30q11, all models show a rapid collapse into a BH within 0.9 ms and form a BH with mass range $M_{\rm BH} = 2.68 - 3.39\,M_\odot$ and dimension-less spin range $\chi_{\rm BH} = 0.66 - 0.79$. Our models also estimated the energy radiated in gravitational waves to be between 0.01 and $0.07\,M_\odot c^2$.

We also investigated the relationship between $M_{\rm BH}$, $\chi_{\rm BH}$, and $E_{\rm GW}$, as well as the mass ratio and initial binary mass. We showed that, as expected, the disc mass and the amount of dynamically ejected matter either increases or decreases, respectively, with an increase of mass ratio and total binary mass.

We reported our estimates for the disc mass and amount of ejected matter and compared them to the literature's current fits. Our models'

estimates of mass ejection agree with the fit, but the amount of disc mass is less than the fit's estimate.

Moreover, we calculated gravitational waves and their spectra. We compared the amplitude spectral density of our models to the KAGRA, aLIGO+, Voyager, Einstein Telescope, and Cosmic Explorer sensitivity curves. We propose a possible feature in the amplitude spectral density that could indicate rapid collapse into a BH following the merger of two neutron stars, and that could be observed using future-planned detectors such as the Einstein Telescope and Cosmic Explorer.

Additionally, from the evolution of the rest-mass density, we discussed the possible impact of initial binary mass and mass ratio on the geometry and mass of the accretion disc that will be formed around the post-merger NS or BH.

ACKNOWLEDGEMENTS

This study is part of the PhD thesis of KAC. This study was supported by the Scientific and Technological Research Council of Turkey (TÜBİTAK 117F188 and 119F077). KAC thanks TÜBİTAK for his Fellowship (2210-C and 2211-A). The work has been performed under Project HPC-EUROPA3 (INFRAIA-2016-1-730897), with the support of the EC Research Innovation Action under the H2020 Programme; in particular, KAC gratefully acknowledges the support of Bruno Giacomazzo, the University of Milano-Bicocca, Department of Physics 'Giuseppe Occhialini' and the computer resources and technical support provided by HPC-CINECA. KY would like to acknowledge the contribution of COST (European Cooperation in Science and Technology) Action CA15117 and CA16104.

DATA AVAILABILITY

The initial data sets we used in these simulations are available in a repository and can be accessed via 10.5281/zenodo.8382258.

REFERENCES

Abbott B. P., et al., 2020, ApJ, 892, L3
Abbott B. P. et al., 2016, Phys. Rev. Lett., 116, 061102
Abbott B. P. et al., 2017a, Phys. Rev. Lett., 119, 161101
Abbott B. P. et al., 2017b, ApJ, 848, L12
Alcubierre M., Brügmann B., Dramlitsch T., Font J. A., Papadopoulos P., Seidel E., Stergioulas N., Takahashi R., 2000, Phys. Rev. D, 62, 044034
Alcubierre M., Brügmann B., Diener P., Koppitz M., Pollney D., Seidel E., Takahashi R., 2003, Phys. Rev. D, 67, 084023
Baiotti L., Hawke I., Montero P. J., Löffler F., Rezzolla L., Stergioulas N., Font J. A., Seidel E., 2005, Phys. Rev. D, 71, 024035
Barack L. et al., 2019, Class. Quantum Gravity, 36, 143001
Baumgarte T. W., Shapiro S. L., 1998, Phys. Rev. D, 59, 024007
Bauswein A., Baumgarte T. W., Janka H.-T., 2013, Phys. Rev. Lett., 111, 131101
Bernuzzi S. et al., 2020, MNRAS, 497, 1488
Binnington T., Poisson E., 2009, Phys. Rev. D, 80, 084018
Borges R., Carmona M., Costa B., Don W. S., 2008, J. Comput. Phys., 227, 3191
Bozzola G., 2021, J. Open Source Softw., 6, 3099
Brandt S. R. et al., 2021, The Einstein Toolkit. Zenodo, Available at: https://zenodo.org/records/5770803
Camilletti A. et al., 2022, MNRAS, 516, 4760
Damour T., 1983, in Lecture Notes in Physics, Vol. 124. Springer-Verlag, Berlin, pp. 59
Damour T., Nagar A., 2009, Phys. Rev. D, 80, 084035
Damour T., Nagar A., 2010, Phys. Rev. D, 81, 084016
De Pietri R., Feo A., Maione F., Löffler F., 2016, Phys. Rev. D, 93, 064047
Dietrich T., Ujevic M., Tichy W., Bernuzzi S., Brügmann B., 2017a, Phys. Rev. D, 95, 024029
Dietrich T., Bernuzzi S., Ujevic M., Tichy W., 2017b, Phys. Rev. D, 95, 044045
Douchin F., Haensel P., 2001, A&A, 380, 151
East W. E., Paschalidis V., Pretorius F., Shapiro S. L., 2016, Phys. Rev. D, 93, 024011
East W. E., Paschalidis V., Pretorius F., Tsokaros A., 2019, Phys. Rev. D, 100, 124042
Endrizzi A., Ciolfi R., Giacomazzo B., Kastaun W., Kawamura T., 2016, Class. Quantum Gravity, 33, 164001
Endrizzi A., Logoteta D., Giacomazzo B., Bombaci I., Kastaun W., Ciolfi R., 2018, Phys. Rev. D, 98, 043015
Etienne Z. et al., 2021, The Einstein Toolkit. Zenodo, Available at: https://zenodo.org/records/4884780
Farrow N., Zhu X.-J., Thrane E., 2019, ApJ, 876, 18
Favata M., 2014, Phys. Rev. Lett., 112, 101101
Flanagan É. É., Hinderer T., 2008, Phys. Rev. D, 77, 021502
Gourgoulhon E., Grandclément P., Taniguchi K., Marck J.-A., Bonazzola S., 2001, Phys. Rev. D, 63, 064029
Gourgoulhon E., Grandclément P., Marck J.-A., Novak J., Taniguchi K., 2016, LORENE: Spectral methods differential equations solver, Astrophysics Source Code Library, record ascl:1608.018
Hawke I., Löffler F., Nerozzi A., 2005, Phys. Rev. D, 71, 104006
Hinderer T., 2008, ApJ, 677, 1216
Hotokezaka K., Kyutoku K., Okawa H., Shibata M., Kiuchi K., 2011, Phys. Rev. D, 83, 124008
Hotokezaka K., Kiuchi K., Kyutoku K., Okawa H., Sekiguchi Y.-i., Shibata M., Taniguchi K., 2013, Phys. Rev. D, 87, 024001
Kashyap R. et al., 2022, Phys. Rev. D, 105, 103022
Kastaun W., Galeazzi F., Alic D., Rezzolla L., Font J. A., 2013, Phys. Rev. D, 88, 021501
Kastaun W., Ciolfi R., Giacomazzo B., 2016, Phys. Rev. D, 94, 044060
Kiuchi K., Sekiguchi Y., Shibata M., Taniguchi K., 2009, Phys. Rev. D, 80, 064037
Kiuchi K., Sekiguchi Y., Shibata M., Taniguchi K., 2010, Phys. Rev. Lett., 104, 141101
Kiuchi K., Kyutoku K., Shibata M., Taniguchi K., 2019, ApJ, 876, L31
Kutta W., 1901, Z. Math. Phys., 46, 435
Kölsch M., Dietrich T., Ujevic M., Brügmann B., 2022, Phys. Rev. D, 106, 044026
Köppel S., Bovard L., Rezzolla L., 2019, ApJ, 872, L16
Löffler F. et al., 2012, Class. Quantum Gravity, 29, 115001
Margalit B., Metzger B. D., 2019, ApJ, 880, L15
Most E. R., Papenfort L. J., Tsokaros A., Rezzolla L., 2019, ApJ, 884, 40
Mösta P. et al., 2013, Class. Quantum Gravity, 31, 015005
Nakamura T., Oohara K., Kojima Y., 1987, Prog. Theor. Phys. Suppl., 90, 1
Nedora V. et al., 2021, Class. Quantum Gravity, 39, 015008
Newman E., Penrose R., 1962, J. Math. Phys., 3, 566
Papenfort L. J., Most E. R., Tootle S., Rezzolla L., 2022, MNRAS, 513, 3646
Paschalidis V., Ruiz M., 2019, Phys. Rev. D, 100, 043001
Perego A., Radice D., Bernuzzi S., 2017, ApJ, 850, L37
Perego A., Logoteta D., Radice D., Bernuzzi S., Kashyap R., Das A., Padamata S., Prakash A., 2022, Phys. Rev. Lett., 129, 032701
Piro A. L., Giacomazzo B., Perna R., 2017, ApJ, 844, L19
Radice D., Perego A., Zappa F., Bernuzzi S., 2018, ApJ, 852, L29
Reisswig C., Pollney D., 2011, Class. Quantum Gravity, 28, 195015
Rezzolla L., Baiotti L., Giacomazzo B., Link D., Font J. A., 2010, Class. Quantum Gravity, 27, 114105
Ruiz M., Tsokaros A., Paschalidis V., Shapiro S. L., 2019, Phys. Rev. D, 99, 084032
Ruiz M., Tsokaros A., Shapiro S. L., 2020, Phys. Rev. D, 101, 064042
Runge C., 1895, Math. Ann., 46, 167
Schnetter E., Hawley S. H., Hawke I., 2004, Class. Quantum Gravity, 21, 1465
Shibata M., Nakamura T., 1995, Phys. Rev. D, 52, 5428
Shibata M., Taniguchi K., 2006, Phys. Rev. D, 73, 064027
Shibata M., Taniguchi K., Uryū K., 2003, Phys. Rev. D, 68, 084020

Shibata M., Taniguchi K., Uryū K., 2005, Phys. Rev. D, 71, 084021
Sun L., Ruiz M., Shapiro S. L., Tsokaros A., 2022, Phys. Rev. D, 105, 104028
Thornburg J., 2003, Class. Quantum Gravity, 21, 743
Tootle S. D., Papenfort L. J., Most E. R., Rezzolla L., 2021, ApJ, 922, L19
Zhang J., Yang Y., Zhang C., Yang W., Li D., Bi S., Zhang X., 2019, MNRAS, 488, 5020

APPENDIX A: ERROR ESTIMATE, MASS CONSERVATION, AND EFFECTS OF ARTIFICIAL ATMOSPHERE'S DENSITY

In Table 2 we reported the values obtained from our simulations run with standard resolution (SR), i.e. with an innermost grid resolution of $dx = 0.16$. To estimate the uncertainty of our numerical results, we performed higher (HR) and lower resolution (LR) simulations for two models using respectively a resolution of $dx = 0.12$ and $dx = 0.20$ on the finest level. To compute our error, we used the method of absolute semi-differences given in equation (A1)

$$Err = \frac{|HR - LR|}{2}, \tag{A1}$$

for models `M32q10` and `M32q11`. Estimated values for our errors are given in Table A1. In the two models, the maximum value of error (last column of Table A1) is considered as an error on related parameters. Note that due to the wide range of masses from 10^{-1} to 10^{-5}, the errors on disc mass and amount of dynamical ejecta are given as uncertainties rather than absolute errors.

We present the baryon mass conservation for models `M28q10`, `M30q10`, and `M32q10` in Fig. A1 and report the values for each model before merger and before BH formation in Table A2. The relative errors on baryon mass conservation before merger and BH formation (or over the entire simulation for models `M28q10` and `M30q11`) are, respectively, below 1.4×10^{-3} and 2.9×10^{-3}. In this case, the disc and ejecta masses used in Table 2 for the models of M32q10 and M32q11 have values smaller than the baryonic mass conservation error. It should be taken into consideration that it is quite possible that the disc and ejecta mass values obtained from these models were affected by the baryonic mass conservation error.

To investigate the effect of artificial atmosphere density on disc mass and ejected matter, we ran simulations with three different artificial atmosphere densities for the model `M32q10` (see Table A3). (1×10^{-9}), (1×10^{-11}), and (5×10^{-12}) for high, standard, and low artificial atmosphere density, respectively. We report that higher NS atmosphere density causes less disc mass and ejecta matter to be measured. On the other hand, if we use half of the standard atmosphere density, there is no difference in the amount of disc mass, but the amount of ejecta varies 1.6 times. As a result, the disc mass should be considered accurate, whereas the ejecta error estimate is larger.

Table A1. Errors on each value given in Table 2 using `M32q10` and `M32q11`. Errors on $M_{\rm disc}$ and $M_{\rm ejec}$ are given as relative errors.

Quantity	`M32q10`	`M32q11`	Max error
$f_{\rm mer}$	0.02	0.02	±0.02
$t_{\rm BH}$	0.002	0.008	±0.008
$M_{\rm BH}$	0.001	0.0001	±0.001
$\chi_{\rm BH}$	0.006	0.003	±0.006
$E_{\rm GW}$	0.002	0.002	±0.002
$M_{\rm disc}$	36(per cent)	17(per cent)	36(per cent)
$M_{\rm ejec}$	96(per cent)	15(per cent)	96(per cent)

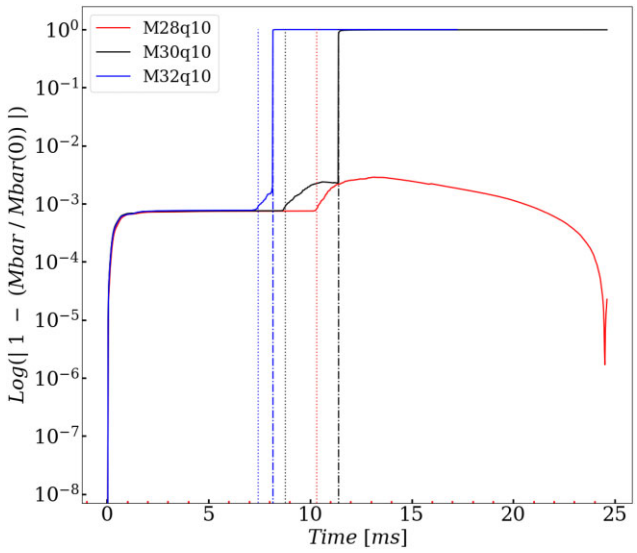

Figure A1. Relative error on the baryon mass conservation for the model `M28q10`, `M30q10`, and `M32q10`. The times of merger and of BH formation, if formed, are shown as vertical dotted and dot-dashed lines.

Table A2. We reported the maximum relative error on the baryon mass for the all models simulated in this paper. The symbol (∗) indicates that the model does not have enough matter to collapse into a BH after the merger. Therefore, we reported the maximum baryon mass error during the whole simulation.

Model	Max value (per cent) $t < t_{\rm mer}$	Max value (per cent) $t < t_{\rm BH}$
`M28q10`	0.08	0.29∗
`M30q10`	0.09	0.24
`M30q11`	0.09	0.26∗
`M32q10`	0.09	0.19
`M32q11`	0.09	0.25
`M32q12`	0.09	0.24
`M32q13`	0.09	0.25
`M32q14`	0.09	0.17
`M32q16`	0.08	0.13
`M32q18`	0.07	0.12
`M32q20`	0.07	0.10
`M34q10`	0.09	0.17
`M36q10`	0.11	0.22
`M36q11`	0.11	0.20
`M38q10`	0.13	0.25
`M38q11`	0.12	0.22
`M40q10`	0.14	0.29
`M40q11`	0.14	0.24

Table A3. Disc and ejecta mass for simulation of the model `M32q10` with high, standard, and low NS atmosphere density values.

Quantity	High (1×10^{-9})	Standard (1×10^{-11})	Low (5×10^{-12})
$M_{\rm disc}$	4.0×10^{-7}	1.1×10^{-4}	1.1×10^{-4}
$M_{\rm ejec}$	4.6×10^{-8}	3.3×10^{-5}	2.0×10^{-5}

This paper has been typeset from a TEX/LATEX file prepared by the author.